Available online at: http://www.iajps.com   *Research Article*

ROLE OF CHEST COMPUTED TOMOGRAPHY SCANS IN THE EVALUATION OF CHEST MORPHOLOGY IN COVID-19 PATIENTS

[1] Ali Mohd Ali Alyami,
[2] Munassar Dakkam Lasloom,
[3] Hashan Dakkam Alsallum,
[4] Essa Alhashlan,
[5] Mohammed Ali Alammari

Abstract:

Objectives: This study aims to demonstrate the role of chest computed tomography scans in the evaluation of chest morphology in patients with a history of COVID-19.

Methodology: This study was conducted at King Khalid Hospital, Najran, Saudi Arabia, from January 2022 to May 2022.

The study sample included 100 patients with positive polymerase chain test, 64 slice units GE Medical Systems were used to examine patients with COVID-19.

Results: 100 patients with a positive polymerase chain for COVID-19 were included. Regarding the signs and symptoms, 48 (48%) of the 100 patients had a fever, and 22 (22%) of the 100 patients had a cough. The most frequent CT abnormalities observed were ground-glass opacity 32 (32%), consolidation (20, 20%), and interlobular septal thickening (17, 17%).

Moreover, The distribution of these findings was most common in the Subpleural zone (55, 55%) and the diffuse zone (31, 31%).

Conclusion: COVID-19 primarily impacts the Subpleural Zone, according to the studies. According to this study, the imaging hallmark of COVID-19 infection is ground-glass opacities and consolidation in the lung periphery. This finding could help physicians with limited healthcare resources predict cases with potentially higher mortality when treating patients.

Keywords: COVID-19, HRCT, Chest

Corresponding author:
Ali Mohd Ali Alyami,

QR code

INTRODUCTION:
1.1. Introduction
In December 2019, a novel coronavirus outbreak broke out in Wuhan (the capital of Hubei Province in central China). Initially, the sick people were thought to have been exposed to the Huanan seafood wholesale market. However, 44 patients with pneumonia of unknown cause were reported to WHO between December 31, 2019, and January 3, 2020 (Organization, 2020). This malady spread quickly throughout China's provinces during the Spring Festival travel boom, and cases were later discovered in 26 countries worldwide (Xu et al., 2020). Globally, 372,757 confirmed cases and 16,231 deaths had been reported as of March 25, 2020 (Organization, 2020).

Although most persons with COVID-19 recover within weeks of becoming ill, others develop post-COVID symptoms. Four weeks after being infected with the virus that causes COVID-19, people might develop a wide range of new, returning, or chronic health problems known as post-COVID disorders. In addition, post-COVID problems can affect patients who did not experience COVID-19 symptoms in the days or weeks following their infection. These diseases might manifest as various sorts and combinations of health problems (Prevention, 2021).

Long COVID, long-haul COVID, post-acute COVID-19, long-term COVID effects, and chronic COVID are used to describe these post-COVID problems. The CDC is working with specialists worldwide to learn more about the short- and long-term health implications of COVID-19, who gets it, and why (Prevention, 2021).

CT is a crucial tool for identifying infected patients and monitoring their progress after treatment. Although the CT findings of COVID-19 pneumonia have been documented in the literature, none of the investigations has excluded individuals with fundamental lung disorders (such as COPD, pulmonary TB, or interstitial lung disease). These disorders may share characteristics and patterns with COVID-19 pneumonia(Xiang, 2020).

This study aims to assess the role of a chest CT scan in evaluating chest shape in individuals with a COVID-19 history.

1.2. Research Problem:
COVID-19 symptoms can last for months at a time. As a result, the virus has the potential to harm the lungs, heart, and brain, increasing the risk of long-term health issues.

Most persons with coronavirus disease 2019 (COVID-19) recover fully within a few weeks. However, some patients, even those with minor forms of the condition, still have symptoms after recovering. The harm to the lungs, heart, and brain can be reduced if potentially life-threatening diseases are detected early following COVID-19.

1.3. General objective:
1.3.1. General objective:
The general objective of this study is to demonstrate the role of chest computed tomography scans in evaluating chest morphology in patients with a history of COVID-19.

1.3.2. Specific objective:
- To detect the findings that occur in patients with a history of COVID-19.
- To determine the distributions of findings according to site.
- To determine the distributions of findings according to age groups.
- To determine the distributions of findings according to gender.

2. THEORETICAL BACKGROUND AND PREVIOUS STUDIES
2.1 Theoretical background
2.1.6 Anatomy of the chest
The upper section of the trunk between the neck and the belly is known as the thorax. The bony thorax, the respiratory system proper, and the mediastinum are the three components of the radiographic anatomy of the chest.

2.1.6.1 Bony thorax
The bony thorax is a portion of the skeletal system that protects the areas of the chest involved in breathing and blood circulation. The phrase "thoracic viscera" refers to the regions of the chest that contain the lungs and the remaining thoracic organs in the mediastinum(Waugh, 2022). The sternum (breastbone), which has three divisions, is found anteriorly in the bony thorax. The manubrium (mah-nu′-bre-um), the body (mah-nu′-bre-um), and the xiphoid process (mah-nu′-bre-um) make up the superior section.

The two clavicles (collarbones) connect the sternum to the two scapulae (shoulder blades), the 12 pairs of ribs that circle the thorax, and the 12 thoracic vertebrae posteriorly make up the bony thorax. (Fig. 2.1)(Waugh, 2022).
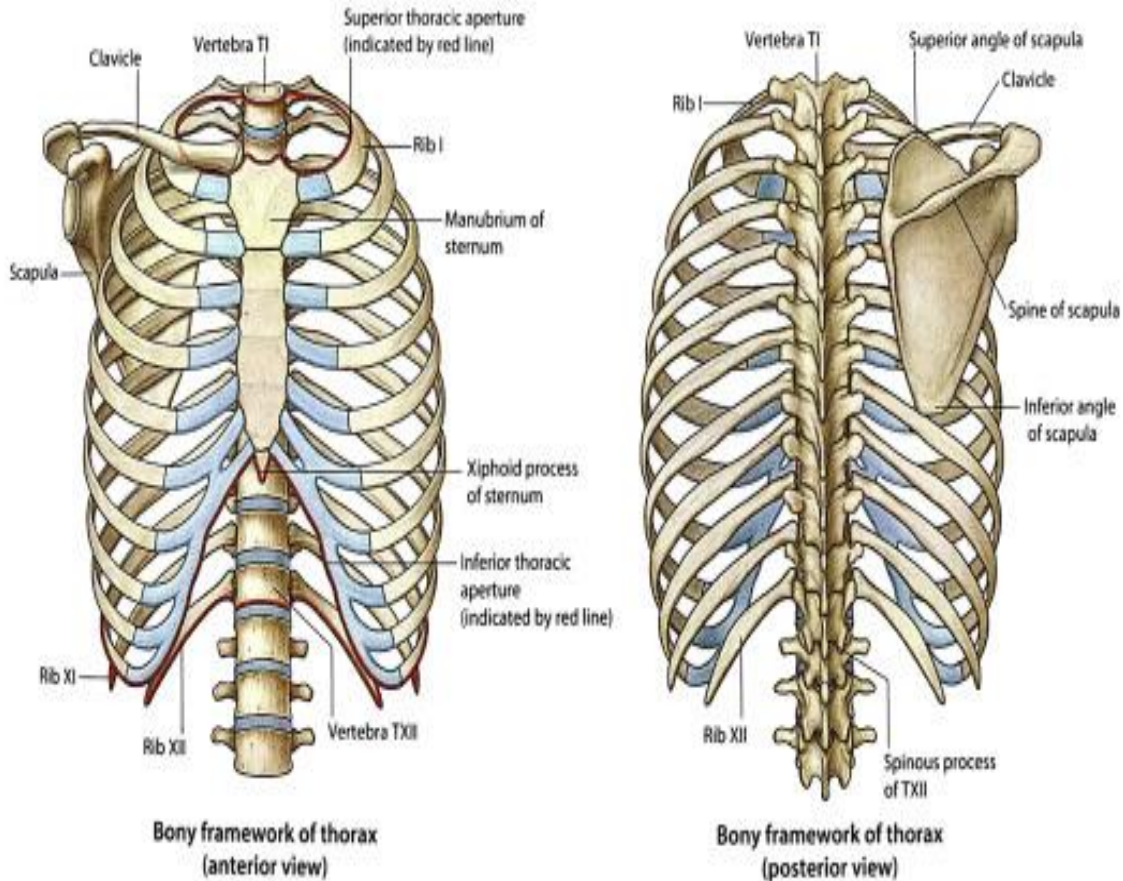
Figure 2.1: Shows the bony thorax(Yang, 2020)

2.1.6.2 Respiratory system

The exchange of gaseous chemicals between the air we breathe and the bloodstream is called respiration. The respiratory system comprises the bodily parts that allow air to pass through as it goes from the nose and mouth to the lungs. The respiratory system is divided into four categories, as shown in Fig. 2.2. The pharynx, trachea, bronchi, and lungs are the pharynx, trachea, and bronchi (Brantigan, 1963).

The dome-shaped diaphragm, the principal muscle of inhalation, is an essential element of the respiratory system. (Brantigan, 1963).

Hemidiaphragms are each half of the diaphragm ("Hemi-" means half). The volume of the thoracic cavity grows as the diaphragm dome goes downward. This increase in volume, together with other thoracic dimensional motions discussed later in this chapter, lowers intra-thoracic pressure, resulting in air being sucked into the lungs through the nose and mouth, pharynx, and larynx, trachea, and bronchi. This promotes inspiration, or the filling of the lungs with air(Waugh, 2022)
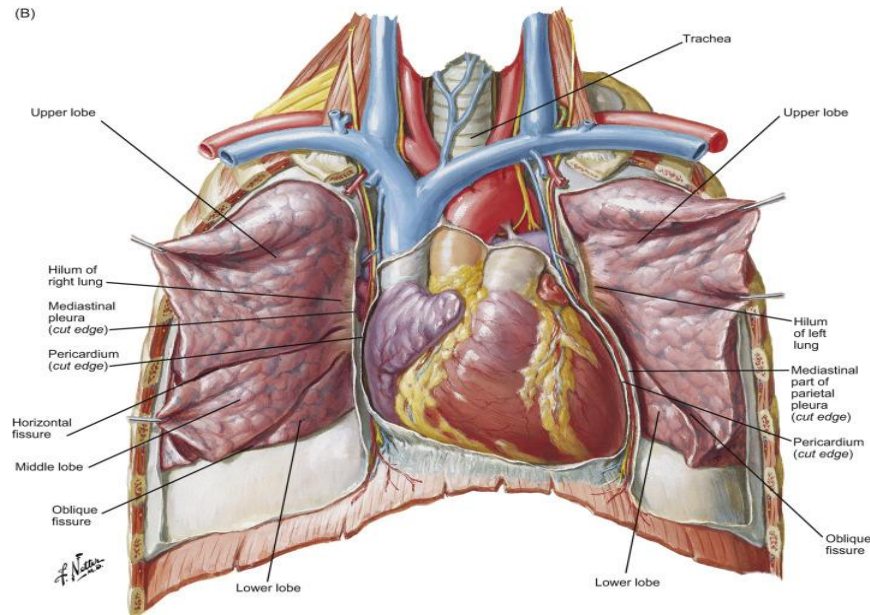
Figure 2.2: Shows the respiratory system(Hansen, 2022).

2.1.6.3 Pharynx

The pharynx (far′-inks) (upper airway) is a critical component in the respiratory system because air must flow through it before entering the respiratory system, which starts with the larynx (voice box). The pharynx is the posterior area between the nose and mouth above and the larynx and oesophagus below, commonly known as the upper airway or upper respiratory tract. (Drake, 2019).

The digestive and respiratory systems share this space since it acts as food, water, and air pathway.
The pharynx has three divisions, as shown in Fig. 2.3: Nasopharynx (na″-zo-far′-inks), oropharynx (o″-to-far′-inks), and laryngopharynx (Lah-ring″-go-far′-inks) are three different parts of the throat. The pharynx communicates with the oesophagus and various cavities in the back of the throat, including the nose (nasopharynx), mouth (oropharynx), and larynx (laryngopharynx). The roof of the oral cavity is made up of hard and soft palates. The uvula (u′-Vu-lah) is the lowest posterior part of the soft palate that marks the nasopharyngeal and oropharyngeal boundaries(Drake, 2019).

From the upper border of the epiglottis (ep″-i-glot′-is) to where the laryngopharynx narrows to reach the oesophagus, the laryngopharynx lies above and posterior to the larynx.

The epiglottis' upper portion projects upward beyond the tongue and serves as a lid or slanted larynx aperture. The epiglottis is down and covers the laryngeal opening during swallowing, preventing food and fluid from entering the larynx and bronchi.

The hyoid bone, thyroid cartilage of the larynx (Adam's apple), thyroid gland, and trachea are also represented in this sectional lateral drawing and detailed in the following sections on the larynx and trachea(Waugh, 2022).
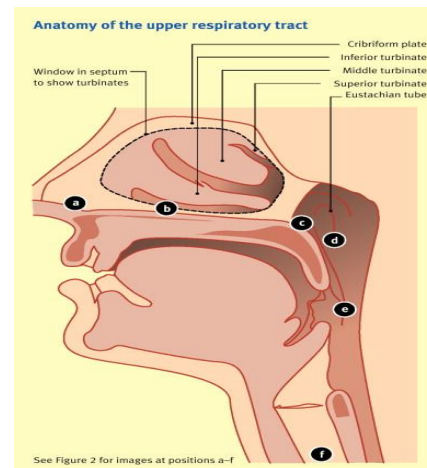

Figure 2.3:Anatomy of the pharynx(Cheesman & Burdett, 2011).

2.1.6.4 Larynx (Voice Box)

In an adult, the larynx is a cage-like cartilaginous structure that measures 1.5 to 2 inches (4 to 5 cm) in length. The larynx is a tiny bone near the front of the neck hanging from the hyoid bone (Fig. 2.4). The hyoid bone is located directly behind the tongue or

mouth floor in the upper neck (see Fig. 2.4). Therefore, the larynx does not include the hyoid bone (Drake, 2019).

The larynx is the organ of speech. As air flows between the vocal cords in the larynx, sounds are produced (Fig. 2.4). C3 is the approximate level of the upper laryngeal edge. Its lower edge, where the larynx connects to the trachea, is at C6.

The larynx comprises cartilages joined by ligaments and moved by several muscles that help with the complicated sound-making or voice process. The thyroid cartilage, which consists of two used plate-like structures that form the anterior wall of the larynx, is the largest and least movable of these cartilages. The laryngeal prominence, often known as Adam's apple, is a conspicuous anterior projection of the thyroid cartilage that may easily be palpated. Because it is easy to find, this large structure serves as a significant positioning landmark. In addition, the thyroid cartilage's laryngeal prominence, found around C5, is a practical topographic reference for detecting specific skeletal elements in this region (Waugh, 2022).

The cricoid cartilage (kriʹ-koid) is a ring of cartilage that forms the larynx's interior and posterior walls. It is linked to the trachea's first cartilage ring.

The epiglottis, which resembles a lea with the narrow distal stem portion linked to a component of the thyroid cartilage, is one of the cartilages that make up the larynx. During swallowing, the epiglottis flips down and covers the trachea, as detailed on the previous page (Fig. 2.5)(Drake, 2019).
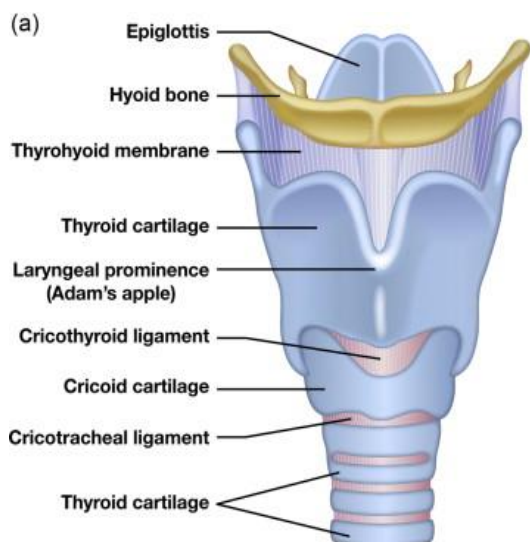
2.1.6.5 Trachea

The trachea, or windpipe, is the second division of the respiratory system proper, continuing downward from the larynx. It is a fibrous muscle tube with a diameter of 3/4 inches (2 cm) and 4.5 inches (11 cm). The front wall has around 16 to 20 C-shaped cartilage rings. The trachea does not collapse during exhalation; therefore, these hard rings maintain the airway open (Bontranger & Lampignano, 2005).

The trachea runs from the level of C6 (sixth cervical vertebra) down to the level of four or five (fourth or fifth thoracic vertebra), where it separates into right and left main bronchi (Bontranger & Lampignano, 2005).

The thyroid, parathyroid, and thymus glands are located near the respiratory system.

The aortic arch's primary arterial branches are shown in Fig. 2.6. The brachiocephalic left common carotid and left subclavian arteries are the main branches. The superior vena cava is a big vein that returns blood to the heart from the head, neck, and upper limbs (Bontranger & Lampignano, 2005).
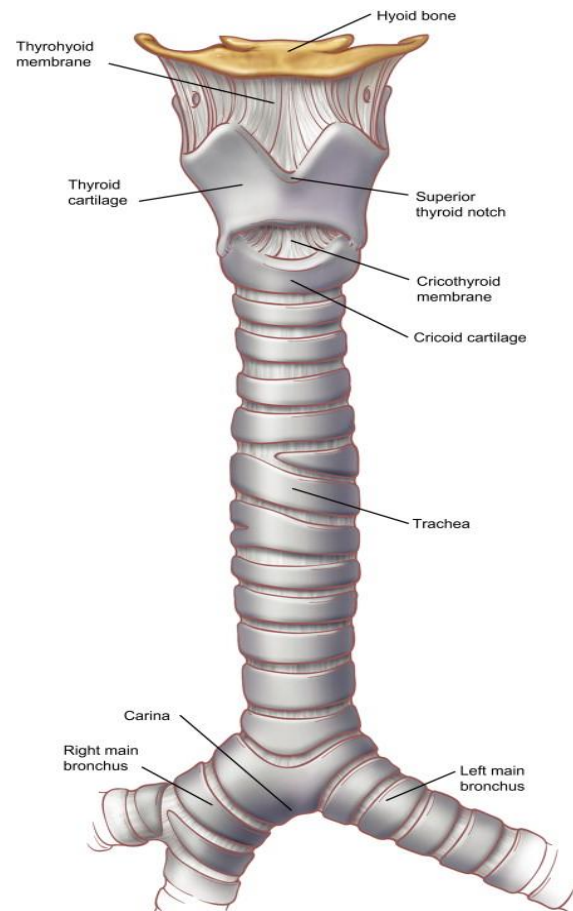

Figure 2.5: Anatomy of the trachea(Minnich & Mathisen, 2007).

Figure 2.4: Anatomy of the larynx(Lott, 2015).

2.1.6.6   Right and Left Bronchi

The right and left primary bronchi, also known as the right and left main stem bronchi, make up the third component of the respiratory system.

The primary bronchus on the right is broader and shorter than the one on the left. In addition, because the angle of divergence from the distal trachea is less abrupt in the right primary bronchus than in the left, the angle of divergence from the distal trachea is less abrupt. Therefore, food particles or other foreign items that enter the respiratory system are more likely to enter and lodge in the right bronchus due to the size and shape difference between the two significant bronchi (Chaudhry & Bordoni, 2022).

The right bronchus is 2.5 centimetres long and 1.3 centimetres wide. The right bronchus' divergence angle is only about 25 degrees (Chaudhry & Bordoni, 2022).

The left bronchus has a smaller diameter (1.1 cm) but is almost twice as long as the right bronchus (5 cm). The left primary bronchus has a divergence angle of around 37°, which is more horizontal than the right bronchus. Food particles and other foreign substances are less likely to enter the let bronchus because of the greater angle and smaller diameter. The carina (Kah-ri′-nah) is a ridge on the lowest tracheal cartilage that may be seen at the bottom and inside of the trachea, separating into right and left bronchi. (Fig. 2.7). When viewed via a bronchoscope, the carina is to the left of the midline, and the right bronchus seems more open than the left, which explains why particles that come down the trachea are more likely to enter the right bronchus. The carina's position, as indicated in Fig. 2.7, the separation into the right and left principal bronchi are at the lower level. This is at the T5 level and is utilized as a specific reference point or CT of the thoracic level (Chaudhry & Bordoni, 2022). Aside from size and shape changes, alveoli, lobes, and secondary bronchi, another significant distinction between the right and left bronchi is that the right divides into three secondary bronchi. In contrast, the left divides into only two, each accessing individual lobes of the lungs (Fig. 2.8). The right lung has three lobes, while the left lung only has two, as is demonstrated in Fig.2-8. These secondary bronchi divide further into smaller branches known as bronchioles, which spread throughout each lobe (Chaudhry & Bordoni, 2022). These little terminal bronchioles lead to alveoli, which are tiny air sacs. There are 500 million to 700 million alveoli in each of the two lungs. The thin walls of the alveoli exchange

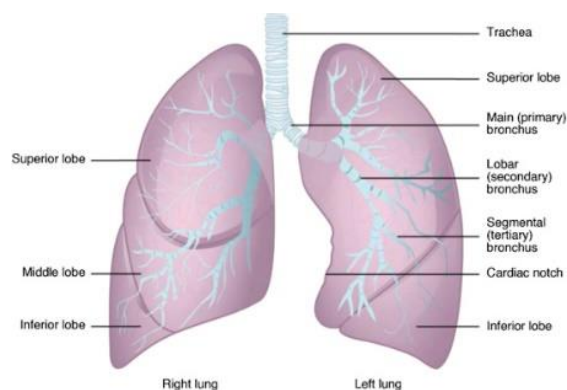oxygen and carbon dioxide in the blood (Chaudhry & Bordoni, 2022)

Figure 2.6: The anatomy of lung bronchi and alveoli(Aung et al., 2019).

2.1.6.7   Lung

The two giant, spongy lungs on each side of the thoracic cavity make up the fourth and final division of the respiratory system. The lungs take up all of the space left by other structures. The superior (upper), middle, and inferior (lower) lobes of the right lung are split by two deep fissures (Chaudhry & Bordoni, 2022). The oblique fissure is the inferior fissure that connects the inferior and middle lobes. A horizontal fissure separates the superior and middle lobes. The superior (upper) and inferior (lower) lobes of the left lung are separated by a single deep oblique fissure (Chaudhry & Bordoni, 2022).

The lungs are made up of parenchyma (pahreng′-ki-mah), a light, spongy, extremely elastic tissue.

This substance allows the breathing mechanism, which involves the expansion and contraction of the lungs, to bring oxygen into the bloodstream and eliminate carbon dioxide through the thin walls of the alveoli (Chaudhry & Bordoni, 2022).

The pleura is a fragile double-walled sac or membrane surrounding each lung and can be seen in both frontal and side views (Fig. 2.10) and sectional (Fig. 2.12) drawings. The parietal pleura is the outer layer of this pleural sac that lines the inner surface of the chest wall and diaphragm. The pulmonary or visceral pleura is the inner layer that covers the surface of the lungs and extends into the gaps between the lobes (see Fig. 2.11). The pleural cavity, or potential space between the double-walled pleura, contains a lubricating fluid that facilitates movement of one or the other while breathing. This area can be visualized radiographically

when a lung collapses or when air or fluid collects between these two layers. The presence of air or gas in this pleural cavity causes a pneumothorax, in which air or gas pressure in the pleural cavity causes the lung to collapse. A hemothorax is caused by an accumulation of fluid in the pleural cavity (pleural effusion) (Chaudhry & Bordoni, 2022).
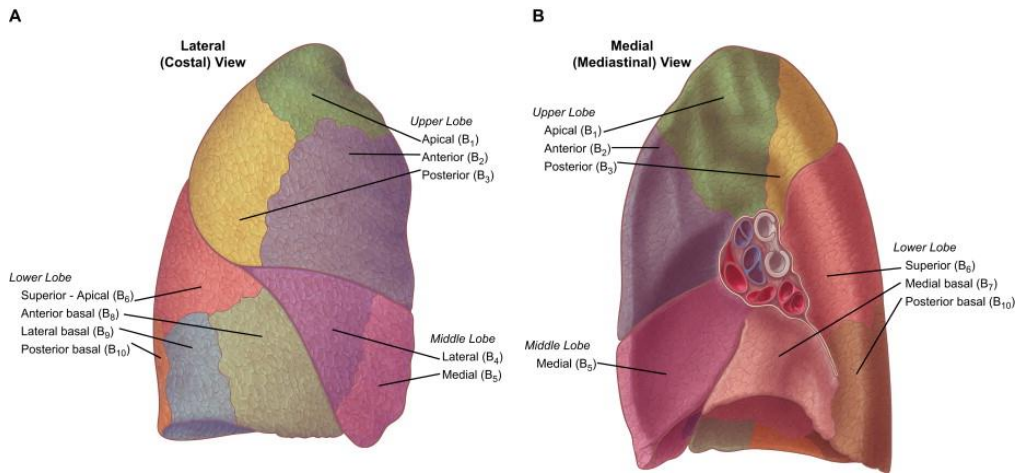

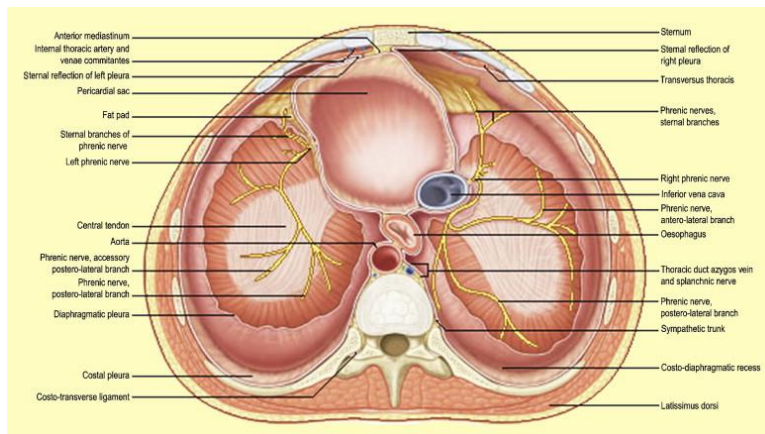**Figure 2.7:** the anatomy of the lobe of the lungs(Aung et al., 2019).

Figure 2.8: Sectional drawing of the lungs and heart(Mahadevan, 2015).
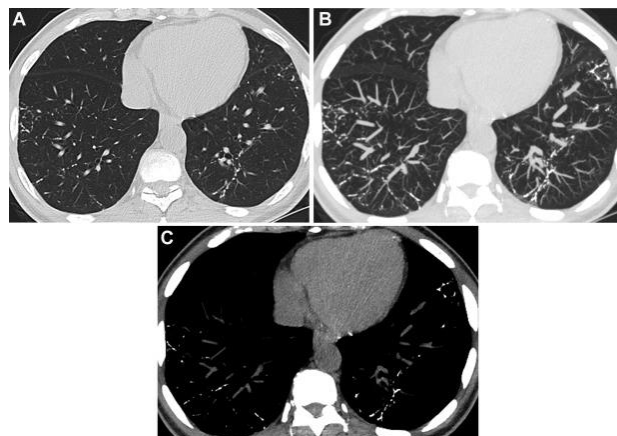

Figure 2.9: Shows an axial CT scan of a lung(Gruden et al., 2020).

2.1.7 Physiology

The lungs are the respiratory system's foundational organs, and their primary role is to promote gas exchange from the environment into the bloodstream (Patton, 2013).

The alveoli transfer oxygen to the capillary network, where it can enter the arterial system and eventually perfuse tissue.

The nose, oropharynx, larynx, trachea, bronchi, bronchioles, and lungs comprise the respiratory system (Patton, 2013).

The lungs have been further divided into lobes, subdivided into around 300 million alveoli. The alveoli are the primary areas of gas exchange. The diaphragm, the major breathing muscle, is innervated by the phoenix nerve. The C3, C4, and C5 nerve roots supply it with information. External intercostals are aspiratory muscles most commonly employed during activity and respiratory distress (Patton, 2013).

2.1.8   Pathology

2.1.8.1   Chronic Obstructive Lung Diseases

Chronic obstructive pulmonary disease (COPD) is a group of respiratory disorders that share a common aetiology mechanism: pathologic restriction of pulmonary airflow (Vijayan, 2013). Chronic bronchitis, bronchiolitis, asthma, cystic fibrosis (CF), bronchiectasis, and α1 antitrypsin deficiency are all disorders. COPD produces gradual and destructive emphysema, recurring inflammation, and loss of lobular tissues and tiny arteries, leading to cor pulmonale due to decreased intrapulmonary blood flow, pulmonary hypertension, and right heart failure (Vijayan, 2013).

2.1.8.2   Pulmonary Infectious Diseases

The etiologic organism's toxicity, replication, persistence and the quality and strength of the host defensive mechanisms all influence the pathologic aspects of lung infections (Krueger, 2013). Suppurative, abscessing, necrotizing, or hemorrhagic bacterial pneumonia (bronchogenic or hematogenous). Viral pneumonia is primarily lymphocytic and, in extreme cases, necrotizing and hemorrhagic (due to immunological T-cell activation) (e.g., classic influenza). Fungal infections in the lungs activate macrophages and frequently result in granulomas (an immunological T-cell reaction); depending on the severity of the infection, they may also induce necrosis and vascular invasion with thrombosis. In addition to parasitic infestations and mycobacterial diseases, granulomas can be caused by phagocytosis. Only acute pneumonia with no significant tissue necrosis can resolve and heal completely (Krueger, 2013). With persistent scarring, longer-lasting or chronic pneumonitides will heal only partially. As a result, chronic, persistent infections increase the likelihood of developing chronic restrictive lung disease(Krueger, 2013).

2.1.8.3   Immunologic Diseases of the Lung

Asthma (COPD) and acute hypersensitivity pneumonitis (an RPD) are two lung illnesses with immunologic aetiology. Similarly, autoimmune processes are thought to have a role in developing and progressing several types of IPF (fibrosing alveolitis) (Riario Sforza & Marinou, 2017). Collagen vascular illnesses like SLE, scleroderma, and rheumatoid arthritis usually affect the lungs. Rheumatoid arthritis patients may develop silicosis (Caplan's syndrome), various systemic vasculitides, such as Goodpasture's syndrome, Wegener's pneumonic granulomatosis, and Churg–Strauss disease, which impact the lungs. Although the visible signs of these illnesses are sometimes nonspecific, the images provide some examples to aid in the differential diagnosis. All are assumed to have an autoimmune origin, while the cause is unknown. Many of these illnesses have genetic characteristics (Riario Sforza & Marinou, 2017).

2.1.8.4   Vascular Diseases of the Lung

Primary or secondary changes in the structure of blood vessels are present in vascular lung disorders. Primary pulmonary glomangiosis (Masshoff and Röher disease [MRD]) and plexiform vascular disease (the end-stage of pulmonary hypertension) are the most prevalent. Another group of vascular diseases in the lungs is caused by clotting disorders, with thromboembolism or local thrombosis occluding intrapulmonary blood arteries (e.g., using hormonal contraceptives)(Lai-Fook, 2006). Cor pulmonale is caused by structural vascular changes, such as widespread thrombosis of tiny arteries, frequently accompanied by significant pulmonary hypertension. Pulmonary hemorrhagic infarction (in cases of left ventricular heart failure) and, eventually, pulmonary hypertension can be caused by thromboembolic and severe thrombotic illnesses. Abrupt pulmonary artery thromboembolism causes acute right heart failure and rapid death (Lai-Fook, 2006).

2.1.8.5   Tumours of the Lungs and Pleura

Lung cancers are epithelial tumours (carcinomas), mesenchymal tumours (sarcomas), and metastases. The origin cell is used to classify everyone (e.g., squamous cell carcinoma [SCC] of the bronchus, adenocarcinoma of the bronchial glands, or the alveolar pneumocytes). Angiosarcomas, neurosarcomas, and lymphosarcomas are all types of

sarcomas. Other cancers include big cell or small cell carcinomas and carcinoids, which are tumours of specialized neuroendocrine cells in the lungs. Finally, tumour metastases from malignancies of the breast, pancreatic, testes, bone, skin (e.g., malignant melanoma), and other sarcomas frequently affect the lungs. Mesenchymal pleural tumours that have been diagnosed as mesothelioma can seem like adenoid epithelial formations (Armitage, 1985).

2.1.9   COVID-19

In severe coronavirus disease 2019 (COVID-19) caused by the new coronavirus SARS-CoV-2, the lung is the most afflicted organ, and lung damage is the leading cause of mortality in most patients (Bösmüller, Matter, Fend, & Tzankov, 2021). The critical aspects of fatal COVID-19 have been characterized by several groups worldwide, primarily based on autopsy reports. Oedema, epithelial destruction, and capillaritis/endothelialitis are common early alterations commonly accompanied by micro thrombosis. In addition, exudative diffuse alveolar damage (DAD) with hyaline membrane formation and pneumocyte type 2 hyperplasia develops in patients with apparent respiratory insufficiency, which can be worsened by superinfection and advance to organizing/fibrotic stage DAD (Bösmüller et al., 2021). On the other hand, these characteristics are not unique to COVID-19 and can be present in a variety of illnesses, including viral infections. Clinically, severe COVID-19 is characterized by a high viral load, lymphopenia, massive secretion of pro-inflammatory cytokines, and hypercoagulability, as evidenced by elevated D-dimers and a higher frequency of thrombotic and thromboembolic events. In contrast, virus loads and cytokine levels tend to decrease in late disease stages as tissue repair, including angiogenesis, takes over. The current review summarizes our current understanding and open questions about the pathophysiology of severe pulmonary COVID-19 based on current literature and the authors' personal experience derived from clinical autopsies and attempts to summarize our current understanding and open questions about the pathophysiology of severe pulmonary COVID-19 based on current literature and the authors'(Bösmüller et al., 2021).

2.1.10   CT Historical Background

David Kuhl and Roy Edwards of the University of Pennsylvania started working on a new approach to using tomographic imaging to identify radioactive isotopes in the body in the late 1950s. Kuhl was a physician who had been interested in radiography since high school and had spent his leisure time in medical school attempting to construct a rectilinear

scanner using the photo recording approach. Edwards was the head of the radiology department's engineering shop (Sostre, Ashare, Quinones, Schieve, & Zimmerman, 1978).

Their tests with Geiger-Muller tubes, a technique developed in the late 1940s, produced a picture like an X-radiograph. This realization inspired them to create the Mark II scanner, which was fully planned by July 1959, under construction by September of that year, and used for emission tomography as early as summer 1963 (Aber, Marzolff, Ries, & Aber, 2019). On 14, They created what is believed to be the first CT (computer tomography) scan of a patient in May 1965. They constructed a CT scanner that employed a computer to analyze x-ray images from various angles to map things blocking the x-rays. The Mark II was a device that performed a transaxial section tomography of a living body using a double-headed scanner. The Mark II captured pictures with an optical integrator rather than a digital computer, unlike later tomography equipment. These detectors captured a basic back projection during their linear movements. Despite this advancement, diagnosticians deemed these images too fuzzy for most medical applications; however, they could aid doctors and scientists in understanding the orientation and geometry of the scanned subject (Garvey & Hanlon, 2002). Godfrey Hounsfield, a British scientist, would perform the first scan of a human patient with a computer that could build a composite image utilizing x-ray input in 1971. Although Hounsfield, who would later share the Nobel Prize for this invention in 1979, was unaware of Kuhl and Edwards' tomography work, his contemporaries did. "The limitation of the scan lines to a single plane allows us to see Kuhl and Edwards' work as an essential predecessor to emission CT," says Steve Webb, a radiological tomography historian (Webb, 1990). Following up on this experiment, Kuhl and Edwards' team developed a series of SPECT (single photon emission computer tomography) systems that could provide a crisper image faster: the Mark III in 1968 and the Mark IV in 1975. Their methods became the standard strategy used by PET scanner manufacturers (Webb, 1990).

2.1.11   CT physics:

David Kuhl and Roy Edwards of the University of Pennsylvania started working on a new approach to using tomographic imaging to identify radioactive isotopes in the body in the late 1950s. Kuhl was a physician who had been interested in radiography since high school and had spent his leisure time in medical school attempting to construct a rectilinear scanner using the photo recording approach. Edwards

was the head of the radiology department's engineering shop (Webb, 1990).

Their trials with Geiger-Muller tubes, a technique developed in the late 1940s, created a picture like an X-radiograph. They exploited this knowledge to create the Mark II scanner, which was fully planned by July 1959, under construction by September of that year, and used for emission tomography as early as summer 1963. They created what was arguably the first CT (computer tomography) scan of a patient on May 14, 1965. They constructed a CT scanner that utilized a computer to analyze x-ray images from various angles to map structures blocking the x-rays. The Mark II was a device that performed a transaxial section tomography of a living body using a double-headed scanner. The Mark II captured pictures with an optical integrator rather than a digital computer, unlike later tomography equipment. These detectors captured a basic back projection during their linear movements. Despite this innovation, diagnosticians deemed these images too grainy for most medical applications; however, they could aid doctors and scientists in interpreting the orientation and geometry of the scanned subject (Aber et al., 2019).

Godfrey Hounsfield, a British scientist, would perform the first scan of a human patient with a computer that could build a composite image utilizing x-ray input in 1971. Although Hounsfield, who would later share the Nobel Prize for this invention in 1979, was unaware of Kuhl and Edwards' tomography work, his contemporaries did. "The limitation of the scan lines to a single plane allows us to see Kuhl and Edwards' work as an essential predecessor to emission CT," says Steve Webb, a radiological tomography historian (Webb, 1990)

Following up on this experiment, Kuhl and Edwards' team developed a series of SPECT (single photon emission computer tomography) systems that could provide a crisper image faster: the Mark III in 1968 and the Mark IV in 1975. Their techniques became the foundation for developing PET scanners (Webb, 1990).

2.1.12   CT Technique
2.1.12.1 Sequential spaced acquisition
HRCT was first designed to improve spatial resolution in first-generation scanners (sequential image acquisition technique) and then employed with identical parameters in second-generation scanners (helical scanners)(Kakinuma et al., 2015). Some institutions still implement this technique to decrease patient radiation exposure, even while scanning in a

multidetector-row CT scanner (MDCT). In addition, if a full three-acquisition HRCT protocol is used, the additional expiratory and prone imaging can be done consecutively in addition to the volumetric inspiratory scan. Thin sections defined as 1.5 mm (due to hardware limitations, the original HRCT technique used in first and second-generation scanners had a thicker definition of thin slices defined as 3.0 mm) interval of 1-2 cm between the two sets of images, the patient radiation dose is lower than volumetric imaging (Kakinuma et al., 2015).

2.1.12.2 Volumetric acquisition
Because MCTs are so standard nowadays, volumetric thin slices have become the norm. Volume imaging with narrower slices enables more detailed pathology diagnosis and reconstruction in any plane (Prionas, Ray, & Boone, 2010).

Thin portions are defined as less than 1.5 mm thick: post-processing: generally 1 mm, but can range from 0.625-1.25 mm Reduces imaging smoothness and boosts spatial resolution with a high-spatial-frequency or sharpening technique (bone algorithm): Streak artefacts are more visible since the structures are crisper and display more detail. The radiation dose to the patient is higher (Prionas et al., 2010).

2.1.12.3 Fundamental technical protocols
The scan period is 0.5-1 second, and the slice thickness is 0.625-1.25 mm. The used kV was 120, while the mAs ranged from 100 to 200. Therefore, it is possible to utilize a 1.5-3 mm collimation and a matrix size of 768×768 or the maximum available. The FOV of 35 cm is used to cover the entire chest area. High spatial frequency is the reconstruction algorithm utilized in chest examinations. The window in question was long (Alsleem, 2020).

2.1.12.4 Patient position
Expiratory HRCT scans in patients with obstructive lung disorders are performed in supine (routinely) or prone (if suspected ILD) positions. The level of inspiration is full inspiration (routinely suggested).

2.1.12.5 Reducing radiation dose
Low-dose CT procedures can be utilized in follow-up scans of known or younger patients, but image quality will worsen. In addition, most patients receive numerous tests for illness surveillance, resulting in significant radiation dose reduction. Therefore, lower mAs (40 mA) are routinely used, as is a sequential spaced acquisition, commonly used for subsequent expiratory and prone scans. Some institutions also use

this technique for the entire inspiration scan in patients who need imaging follow-up (Kubo et al., 2016).

2.2   Previous Studies

The chest CTs of 121 symptomatic patients infected with coronavirus disease-19 (COVID-19) from four centres in China were reviewed for common CT findings concerning the time between symptom onset and the initial CT scan (i.e. early, 0-2 days (36 patients), intermediate, 3-5 days (33 patients), and late, 6-12 days (25 patients) in a retrospective study conducted by Adam Bernheim et al. On imaging, bilateral and peripheral ground-glass and consolidative pulmonary opacities were the hallmarks of COVID-19 infection. Notably, the CT scans of 20/36 (56%) of the early patients were regular. However, CT abnormalities such as consolidation, bilateral and peripheral illness, increased total lung involvement, linear opacities, "crazy-paving" pattern, and the "reverse halo" sign were more common as time passed following the onset of symptoms. In addition, 10/36 early patients (28%) had bilateral lung disease, 25/33 middle patients (76%) had bilateral lung involvement, and 22/25 late patients had bilateral lung involvement (88 per cent)(Bernheim et al., 2020).

This work by Ran Yang et al. offers a simple semi-quantitative method for determining the severity of COVID-19 in initial chest CT scans. In our sample, a CT-SS score of less than 19.5 may rule out severe or critical manifestations of the disease, with a 96.3 per cent negative predictive value. CT-SS could speed up the triage of patients who need to be admitted to the hospital.

We believe that such an approach might be practical in situations when there are a large number of patients and limited healthcare resources or polymerase chain reaction testing capabilities.

The most frequently involved sites in COVID-19 were the posterior segment of the upper lobe (left, 68 of 102; right, 68 of 102), a superior segment of the lower lobe (left, 79 of 102; right, 79 of 102), lateral basal segment (left, 79 of 102; right, 70 of 102), and posterior basal segment of the lower lobe (left, 81 of 102; right, 83 of 102). In comparison to the middle-upper lobes, lower lobe opacification was more common. There were no significant changes in disease distribution between the right and left lungs. Severe COVID-19 had higher individual scores in each lung compared to moderate instances and a higher total CT-SS (P, .05). With 83.3 per cent sensitivity and 94 per cent specificity, the best CTSS threshold for detecting severe COVID-19 was 19.5 (area under curve = 0.892)(Yang, 2020).

D.J. Lieuwe and colleagues Based on these preliminary findings, we conclude that compliance and lung weight estimation are unrelated in COVID-19-related ARDS patients. Most patients had mixed traits and could not be categorized as either "H" or "L" subphenotypes. On chest CT imaging, patients usually had significant parenchymal involvement and a non-focal morphology, indicating recruitable lung tissue. The respiratory system compliance was similar to that reported in previous COVID-19 patient cohorts (14–16), and ARDS was not associated with COVID-19. For example, in the LUNG-SAFE research and other observational and interventional investigations, the mean Crs was 40-50 mL/cmH2O (Gattinoni et al., 2006).

Due to the lack of quantitative analysis, our findings are limited. Due to the pressing need for data, we used a semi-quantitative surrogate that should capture the differences stated in previous papers. Another disadvantage is the lack of a formal assessment of recruit ability using CT imaging at various PEEP levels. We should realize that most clinicians caring for COVID-19 patients do not have access to semi-quantitative CT-image analysis at a single PEEP level. As a result, most physicians will rely on Crs when these subphenotypes are used in clinical practice. Our findings clearly show that lung compliance does not correspond with the quantity of impacted lung parenchyma. Our data does not show that the "H/L-phenotyping" paradigm adequately defines our patients despite our limited sample size. COVID-19 (Bos, Paulus, Vlaar, Beenen, & Schultz, 2020).

METHODOLOGY:

3.1 Materials:

3.1.1 Population and sampling of study:

We will assess 100 patients with positive PCR in this trial; all patients will get a chest CT scan. Finally, all patients with PCR results that are negative will be excluded.

3.1.2 Area of study:

This study was conducted in the Radiology department, Najran, Saudi Arabia.

3.1.3 Duration of study:

This study was conducted over five months, from January to May 2022.

3.1.4 Equipment and technique:

GE Optima with 64 slice detectors was used to perform a chest CT scan.

CT technical parameters included: matrix 512 X 512, a field of view (FOV) 20 cm; tube current 300 mAs at 120kV; table feed 10mm/rotation, pitch 10/40 mm.

A 3-5 mm cut was performed from the level just below the diaphragm to the mid of the liver to visualize the liver.

3.2 Methods:

3.2.1 Design of study:

This was anticipated to be a descriptive retrospective study.

3.2.2 Variables of study:

Patient age, gender, signs and symptoms, CT findings, and distribution zone are among the study's variables.

3.2.3 Data analysis:

Data management and analysis were performed using SPSS version 20 (IBM Corp., Armonk, NY, USA).

Descriptive analysis and correlation analysis with demographic data will be performed for each objective.

3.2.4 Ethical considerations:

3.2.4.1Informed Consent

The study's goal, funding, how the findings will be utilized, if there are any potential negative consequences of their involvement, and who will have access to the findings will all be disclosed to participants.

RESULTS:

4.1 RESULTS

Table 4.1: Demonstrate the demographic data in this study.

	Frequency	Minimum	Maximum	Mean	Std. Deviation
Age	100	15	88	45.68	16.362

Figure 4.1: shows the distribution of patients in this study.
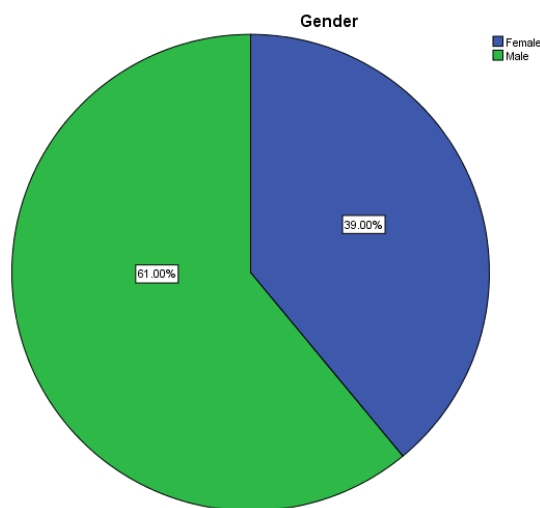
One hundred participants (61 male, 39 female; mean age, 45.6 years ± 16.3; age range, 15–88 years) were enclosed in tables 4.1 and 4.2.

Table 4.2: Demonstrate the distribution of COVID-19 cases concerning age groups

		Frequency	Per cent
Valid	≤19	2	2
	20-29	18	18
	30-39	19	19
	40-49	19	19

	50-59	15	15
	60-69	19	19
	70-79	4	4
	≥80	4	4
	Total	100	100
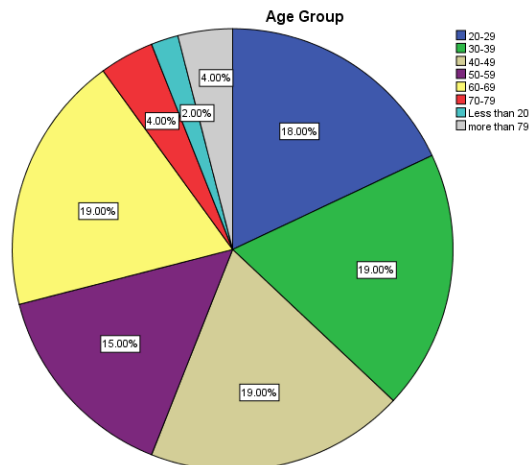
Figure 4.2: shows the distribution of COVID-19 cases concerning age groups.

Patients in this study were classified into ten groups according to age. Groups three, four, and six included the highest number of patients between 30-39, 40–49, and 60–69 years old.

Table 4.3: Demonstrate the history of patients.

History of COVID-19			
		Frequency	Per cent
Valid	No	92	92
	Yes	8	8
	Total	100	100

In table 4.2 and figure 4.3concerning the clinical history, 8 (8%) of 100 patients had a history of covid-19 infection.
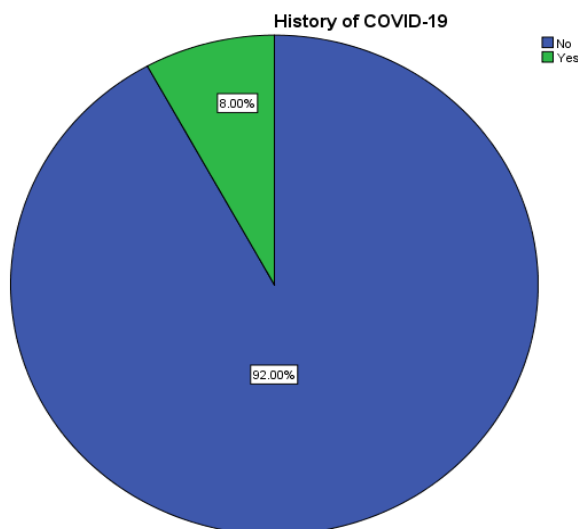
Figure 4.3:shows the history of patients in this study.

Table 4.4: Demonstrate the comorbidity factors in this study

Comorbidity		Frequency	Per cent
	Asthma	5	5
	COPD	5	5
	Diabetes	9	9
Valid	Heart disease	3	3
	Hypertension	12	12
	None	66	66
	Total	100	100
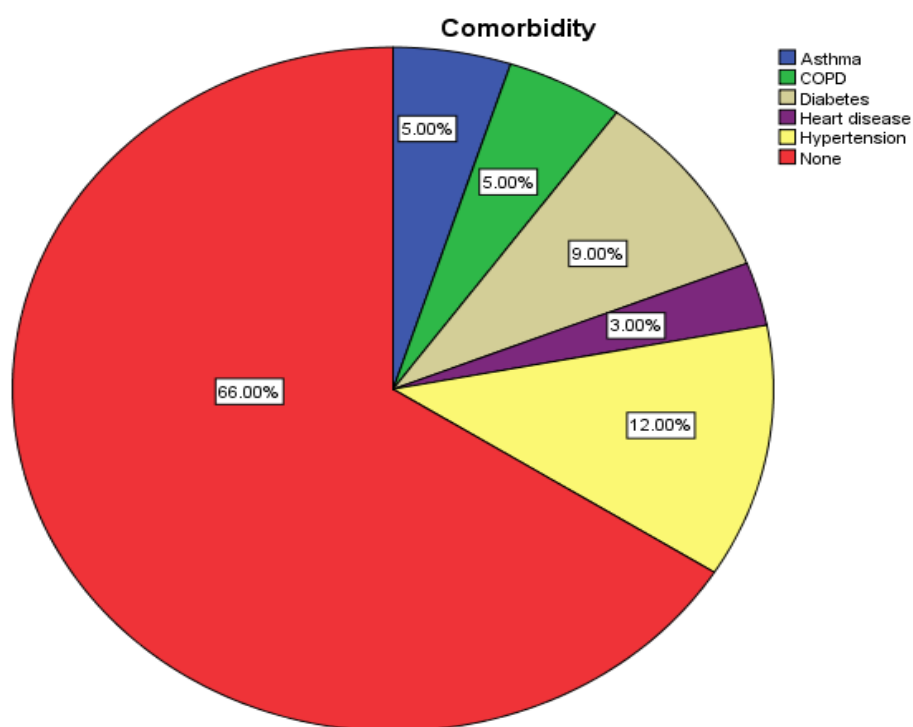
Figure 4.4: shows the comorbidity factors in this study.

Five comorbidity factors were included in the study (asthma, heart disease, diabetes, COPD, and hypertension); Hypertension and Diabetes were associated with the most significant Comorbidity factors.

Table 4.5: Demonstrate patients complaining (signs and symptoms of the COVID-19)

Signs and Symptoms			
		Frequency	Per cent
Valid	Abdominal pain and diarrhoea	11	11
	Chest pain	8	8
	Cough	22	22
	Dizziness and headache	10	10
	Dyspnea	1	1
	Fever	48	48
	Total	100	100
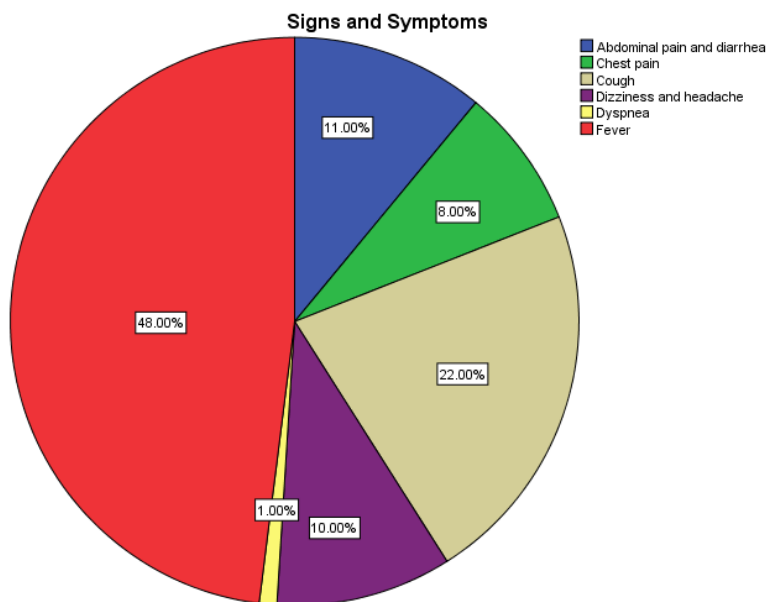
Figure 4.5:shows patients complaining (signs and symptoms of the COVID-19)

Signs and Symptoms, a total of 48 (48%) of patients had a fever, 31 (31%) of patients had signs and symptoms related to respiratory systems,11 (11%) of patients had signs and symptoms related to gastrointestinal track system, and 10 (10%) of patients had dizziness and headache (Table 4.3 and Figure 4.5)

Table 4.6: Demonstrate the chest CT findings for patients diagnosed with COVID-19

CT Findings		Frequency	Per cent
	Consolidation	20	20
	Crazy paving pattern	9	9
	Ground glass opacity	32	32
	Interlobular septal thickening	17	17
Valid	Pericardial effusion	5	5
	Pleural effusion	7	7
	Spider web sign	10	10
	Total	100	100

Ground glass opacity (GGO) and consolidation are the most CT Chest findings that have been reported in all patients with positive COVID-19 cases. Other findings include Interlobular septal thickening (17%), Crazy paving pattern (9%), pericardial effusion (5%), and Spider web sign (10%).
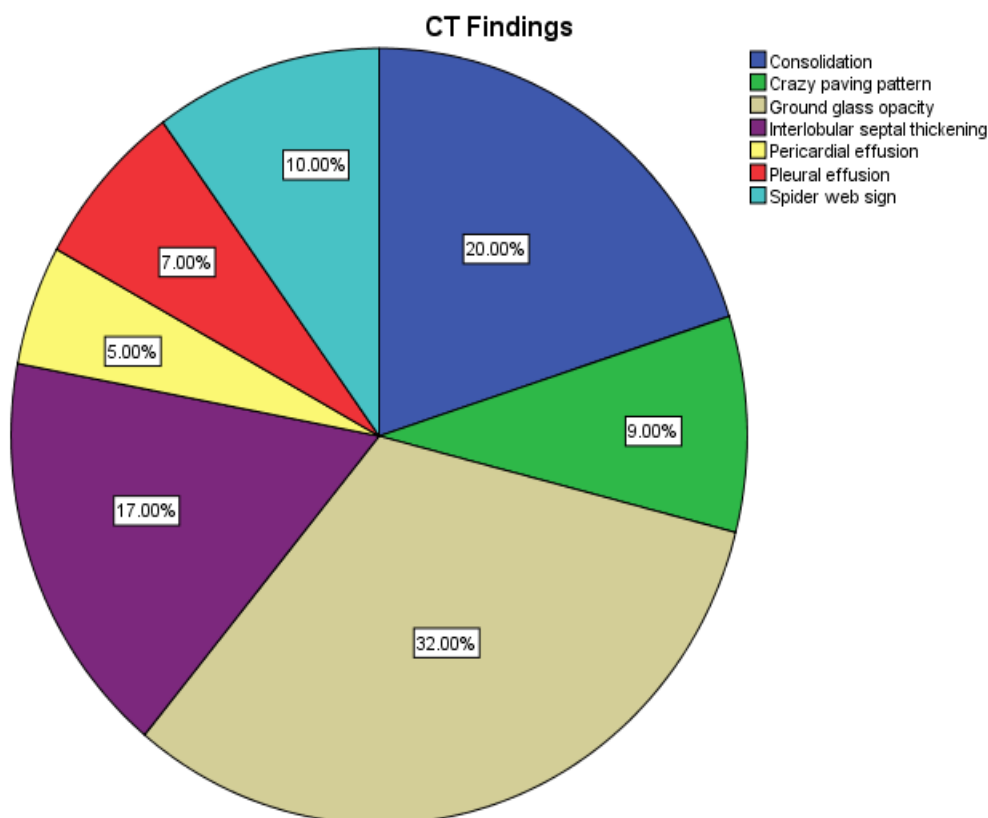
Figure 4.6: Shows the chest CT findings for patients diagnosed with COVID-19

Table 4.7: Demonstrate the chest CT findings distribution for patients diagnosed with COVID-19 diseases

Findings Distribution			
		Frequency	Per cent
Valid	Diffuse distribution	31	31
	Mixed distribution	6	6
	Peribronchial distribution	8	8
	Subpleural distribution	55	55
	Total	100	100

The following chest findings were primarily distributed in the Subpleural area with a percentage (55%) followed by diffuse distribution in the lungs (31%), Peribronchial location (8%), and Mixed (6%)
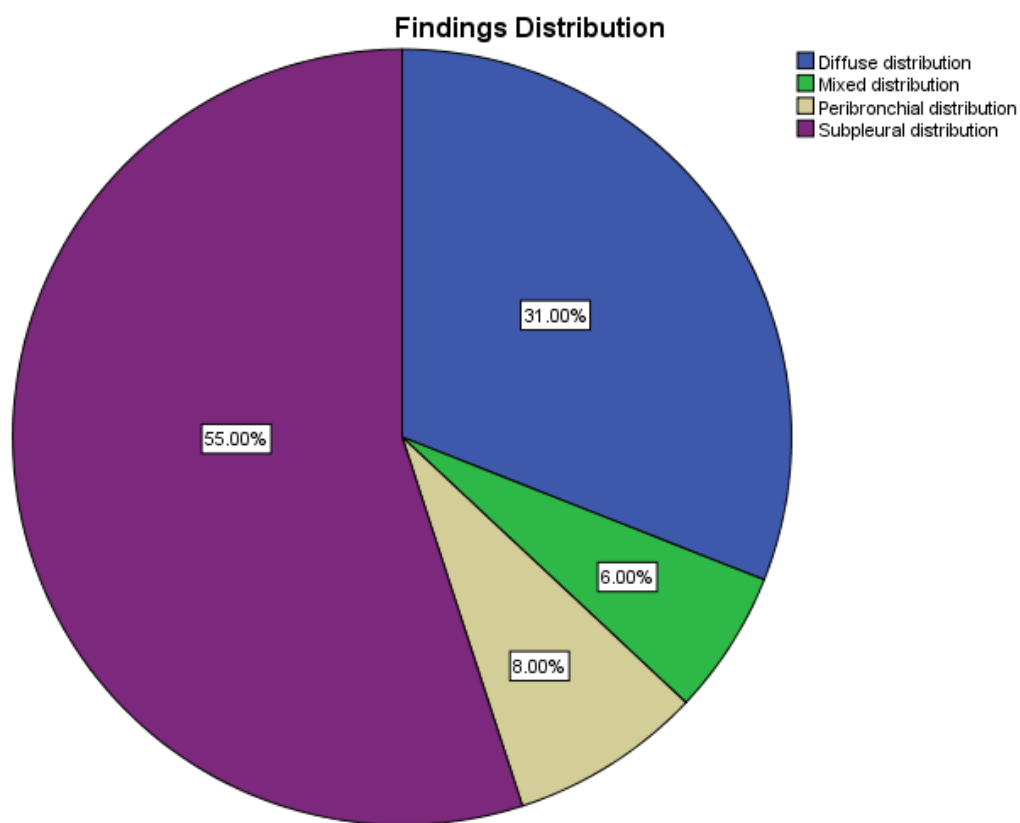

Figure 4.7: shows the chest CT findings distribution for patients diagnosed with COVID-19 diseases.

Table 4.8: Demonstrates the distribution of CT findings according to gender

		CT Findings							Total
		Consolidation	Crazy paving pattern	Ground glass opacity	Interlobular septal thickening	Pericardial effusion	Pleural effusion	Spider web sign	
Gender	Female	7	1	14	9	0	1	7	39
	Male	13	8	18	8	5	6	3	61
Total		20	9	32	17	5	7	10	100

Table 4.9: Demonstrates the distribution of CT findings according to age Group

		CT Findings							Total
		Consolidation	Crazy paving pattern	Ground glass opacity	Interlobular septal thickening	Pericardial effusion	Pleural effusion	Spider web sign	
Age Group	≤20	1	0	1	0	0	0	0	2
	20-29	2	2	7	3	2	0	2	18
	30-39	5	2	5	3	2	1	1	19
	40-49	4	0	8	1	0	2	4	19
	50-59	3	2	2	5	0	1	2	15
	60-69	4	1	6	4	1	3	0	19
	70-79	0	1	1	1	0	0	1	4
	≥80	1	1	2	0	0	0	0	4
Total		20	9	32	17	5	7	10	100

Table 4.10: Demonstrates the distribution of CT findings according to gender

		Findings Distribution				Total
		Diffuse distribution	Mixed distribution	Peribronchial distribution	Subpleural distribution	
Gender	Female	12	2	5	20	39
	Male	19	4	3	35	61
Total		31	6	8	55	100

Table 4.11: Demonstrates the distribution of CT findings according to gender

		Findings Distribution				Total
		Diffuse distribution	Mixed distribution	Peribronchial distribution	Subpleural distribution	
Age Group	≤19	1	1	0	0	2
	20-29	6	1	0	11	18
	30-39	6	0	1	12	19
	40-49	5	0	2	12	19
	50-59	5	1	0	9	15
	60-69	3	3	4	9	19
	70-79	3	0	1	0	4
	≥80	2	0	0	2	4
Total		31	6	8	55	100

DISCUSSION, CONCLUSION, AND RECOMMENDATIONS:

5.1. Discussion

Early diagnosis, triage of patients likely to require intensive care, and detection of arterial and venous thrombosis exacerbating the disease have all been made possible by radiology (mainly chest radiography and CT) in nations with well-developed healthcare systems. In this retrospective analysis, we wanted to show how vital chest computed tomography scans are in evaluating chest morphology. We looked at 100 patients with a positive polymerase chain reaction (PCR) (Table 4.1).

Males were more affected than females when COVID-19 patients were studied, as demonstrated in (Figure 4.1). This is due to men having higher smoking and drinking rates than women. Furthermore, women were more culpable than men in the COVID-19 epidemic. Our findings are consistent with George M. Bwire's epidemiological findings, which indicated that males are more affected by COVID-19 than females in different parts of the world (Bwire, Majigo, Njiro, & Mawazo, 2021).

To our knowledge, being older has always been considered a substantial risk factor for COVID-19. The increased relative risk could be due to long-term exposure to chronic environmental variables.

In the current investigation, we discovered that patients over the age of 40 had a higher COVID-19 incidence rate (42%) than the other age groups (Table 4.2)—our findings on the influence of age matched those of Kalantari, Hamidreza, and colleagues.

According to Kalantari, Hamidreza, and colleagues, the age group 50–59 had the most significant number of probable COVID-19 cases. RT-PCR verified that 102 of 161 probable cases in the 50–59 year age range were positive (Kalantari, Tabrizi, & Foroohi, 2020). Furthermore, our research discovered the following common clinical traits in these patients that were linked to their complaints: Fever (n=48; 48%), cough (n=22; 22%), and abdominal pain and diarrhoea (n=8; 16%) were the most common symptoms (Table and Figure 4.5). When it comes to symptoms and clinical aspects, our findings match those of a study (Kanne, 2020; Song et al., 2020; Wu et al., 2020). To show the features and clinical manifestations of the 80 COVID-19 patients, they discovered that the most common classic COVID-19 symptoms include fever, cough, and muscle discomfort. However, many people do not have all of the symptoms.

Our findings suggested that chest CT might be used to assess illness severity and could be helpful in clinical practice. The most prevalent CT abnormality was GGO, followed by consolidation and interlobular septal thickening (Table and Figure 4.6). This is consistent with the results of the recently published studies(Kanne, 2020; Song et al., 2020; Wu et al., 2020).

The Spider web sign was occasionally visible, but pleura effusion and pericardial effusion were uncommon. The "crazy paving pattern" seen in some GGOs was characterized by reticular interlobular septal thickening. It was caused by alveolar oedema and interstitial inflammation of acute lung damage, as seen in SARS cases. To the best of our knowledge, the spread of lung abnormalities grew throughout the COVID-19 disease. Our data show that lung anomalies were primarily found in the subpleural zones. The lungs had bilateral involvement earlier in the disease, and the peribronchial zones were more frequently implicated (8 per cent). The lung anomalies spread from the periphery to the centre, resulting in a 6 per cent diffuse pattern. (Table 4.5).

Moreover, they report the difference in findings concerning age and gender (Tables4.8 and 4.9). Our research revealed that specific findings are more common in males and older patients.

This gender component and higher rates of most diseases in men could be linked to a general demographic reality in China and around the world: men have a lower life expectancy than women.

Furthermore, our findings revealed that the distribution of discoveries had a more significant impact on the Subpleural zone in both males and females (Tables 4.10). This may serve as a reminder to radiologists to pay special attention to these findings when assessing the imaging of these populations; nevertheless, further research is needed before a definitive conclusion can be reached.

5.2. CONCLUSION:

Finally, we discovered that COVID-19 primarily impacts the Subpleural zone, consistent with earlier research. The imaging characteristic of COVID-19 infection, according to our findings, is ground-glass opacities and consolidation in the lung periphery. Finally, in the correct clinical scenario, detection of this pattern of chest involvement is strongly indicative of COVID-19 infection. Furthermore, the link between dyspnea and significant GGO on imaging may suggest that dyspnea is associated with a worse

prognosis than cough or fever. This discovery could help medical professionals with limited healthcare resources forecast situations with a potentially poorer prognosis when triaging patients. Overall, imaging is beneficial for early detection of disease and follow-up and assessing disease severity; nevertheless, further research is needed to shed light on the disease's radio-clinical link.

5.3. Limitations
For starters, this study had several limitations; the sample size was relatively tiny. Furthermore, we only looked at the first CT scans taken on admission, and the results were not controlled for the exact number of days after symptom onset. In addition, the study's retrospective design may have resulted in selection bias. Another significant problem was that lab testing, and patient outcomes were unavailable in most cases.

5.4. Recommendation:
1. I am emphasizing the appropriate use of CT in managing a patient with COVID-19.
2. Larger sample sizes provide more accurate mean values, identify outliers that could skew the data in a smaller sample, and provide a minor margin error.

REFERENCES:
1. Aber, J. S., Marzolff, I., Ries, J. B., & Aber, S. E. W. (2019). Chapter 6 - Cameras for SFAP. In J. S. Aber, I. Marzolff, J. B. Ries, & S. E. W. Aber (Eds.), *Small-Format Aerial Photography and UAS Imagery (Second Edition)* (pp. 77-92): Academic Press.
2. Alsleem, H. A. A. H. M. (2020). The Feasibility of Contrast-to-Noise Ratio on Measurements to Evaluate CT Image Quality in Terms of Low-Contrast Detailed Detectability. *Medical Sciences Medical Sciences, 8*(3), 26.
3. Armitage, P. (1985). Multistage models of carcinogenesis. *Environ Health Perspect, 63*, 195-201. doi:10.1289/ehp.8563195
4. Aung, H. H., Sivakumar, A., Gholami, S. K., Venkateswaran, S. P., Gorain, B., & Shadab. (2019). Chapter 1 - An Overview of the Anatomy and Physiology of the Lung. In P. Kesharwani (Ed.), *Nanotechnology-Based Targeted Drug Delivery Systems for Lung Cancer* (pp. 1-20): Academic Press.
5. Bernheim, A., Mei, X., Huang, M., Yang, Y., Fayad, Z. A., Zhang, N., . . . Chung, M. (2020). Chest CT Findings in Coronavirus Disease-19 (COVID-19): Relationship to Duration of Infection. *Radiology, 295*(3), 200463. doi:10.1148/radiol.2020200463
6. Bontranger, K. L., & Lampignano, K. L. B. J. P. (2005). *Textbook of radiographic positioning and related anatomy*. St. Louis, MO.: Elsevier Mosby.
7. Bos, L. D. J., Paulus, F., Vlaar, A. P. J., Beenen, L. F. M., & Schultz, M. J. (2020). Subphenotyping Acute Respiratory Distress Syndrome in Patients with COVID-19: Consequences for Ventilator Management. *Annals of the American Thoracic Society, 17*(9), 1161-1163. doi:10.1513/AnnalsATS.202004-376RL
8. Bösmüller, H., Matter, M., Fend, F., & Tzankov, A. (2021). The pulmonary pathology of COVID-19. *Virchows Arch, 478*(1), 137-150. doi:10.1007/s00428-021-03053-1
9. Brantigan, O. C. (1963). *Clinical anatomy*. New York: Blakiston Division, McGraw-Hill.
10. Bwire, G. M., Majigo, M. V., Njiro, B. J., & Mawazo, A. (2021). Detection profile of SARS-CoV-2 using RT-PCR in different types of clinical specimens: A systematic review and meta-analysis. *J Med Virol, 93*(2), 719-725. doi:10.1002/jmv.26349
11. Chaudhry, R., & Bordoni, B. (2022). Anatomy, Thorax, Lungs *StatPearls*. Treasure Island (FL): StatPearls Publishing

12. Copyright © 2022, StatPearls Publishing LLC.
13. Cheesman, K., & Burdett, E. (2011). Anatomy of the nose and pharynx. *Anaesthesia & Intensive Care Medicine, 12*(7), 283-286. doi:https://doi.org/10.1016/j.mpaic.2011.04.013
14. Drake, R. L. (2019). *Gray's anatomy for students and Paulsen : Sobotta, Atlas of anatomy*.
15. Garvey, C. J., & Hanlon, R. (2002). Computed tomography in clinical practice. *BMJ (Clinical research ed.), 324*(7345), 1077-1080. doi:10.1136/bmj.324.7345.1077
16. Gattinoni, L., Caironi, P., Cressoni, M., Chiumello, D., Ranieri, V. M., Quintel, M., . . . Bugedo, G. (2006). Lung recruitment in patients with the acute respiratory distress syndrome. *N Engl J Med, 354*(17), 1775-1786. doi:10.1056/NEJMoa052052
17. Gruden, J. F., Naidich, D. P., Machnicki, S. C., Cohen, S. L., Girvin, F., & Raoof, S. (2020). An Algorithmic Approach to the Interpretation of Diffuse Lung Disease on Chest CT Imaging: A Theory of Almost Everything. *Chest, 157*(3), 612-635. doi:https://doi.org/10.1016/j.chest.2019.10.017
18. Hansen, J. T. M. C. A. G. D. M. G. (2022). *Netter's anatomy colouring book*.
19. Kakinuma, R., Moriyama, N., Muramatsu, Y., Gomi, S., Suzuki, M., Nagasawa, H., . . . Asamura, H. (2015). Ultra-High-Resolution

Computed Tomography of the Lung: Image Quality of a Prototype Scanner. *PloS one, 10*(9), e0137165-e0137165. doi:10.1371/journal.pone.0137165

20. Kalantari, H., Tabrizi, A. H. H., & Foroohi, F. (2020). Determination of COVID-19 prevalence with regards to the age range of patients referring to the hospitals located in western Tehran, Iran. *Gene Rep, 21*, 100910. doi:10.1016/j.genrep.2020.100910

21. Kanne, J. P. (2020). Chest CT Findings in 2019 Novel Coronavirus (2019-nCoV) Infections from Wuhan, China: Key Points for the Radiologist. *Radiology, 295*(1), 16-17. doi:10.1148/radiol.2020200241

22. Krueger, G. R. F. B. L. M. (2013). *Atlas of Anatomic Pathology with Imaging: a Correlative Diagnostic Companion.*

23. Kubo, T., Ohno, Y., Takenaka, D., Nishino, M., Gautam, S., Sugimura, K., . . . i, L. s. g. (2016). Standard-dose vs low-dose CT protocols in the evaluation of localized lung lesions: Capability for lesion characterization-iLEAD study. *European journal of radiology open, 3*, 67-73. doi:10.1016/j.ejro.2016.03.002

24. Lai-Fook, S. J. (2006). STRESS DISTRIBUTION IN THE LUNG. In G. J. Laurent & S. D. Shapiro (Eds.), *Encyclopedia of Respiratory Medicine* (pp. 124-131). Oxford: Academic Press.

25. Lott, D. G. (2015). Chapter 47 - Tissue Engineering of Larynx. In A. Vishwakarma, P. Sharpe, S. Shi, & M. Ramalingam (Eds.), *Stem Cell Biology and Tissue Engineering in Dental Sciences* (pp. 625-640). Boston: Academic Press.

26. Mahadevan, V. (2015). Anatomy of the heart. *Surgery (Oxford), 33*(2), 47-51. doi:https://doi.org/10.1016/j.mpsur.2014.12.001

27. Minnich, D. J., & Mathisen, D. J. (2007). Anatomy of the Trachea, Carina, and Bronchi. *Thoracic Surgery Clinics, 17*(4), 571-585. doi:https://doi.org/10.1016/j.thorsurg.2006.12.006

28. Organization, W. H. (2020). *Novel Coronavirus (2019-nCoV) SITUATION REPORT - 1.* Retrieved from https://www.who.int/docs/default-source/coronaviruse/situation-reports/20200121-sitrep-1-2019-ncov.pdf?sfvrsn=20a99c10_4.

29. Patton, K. T. T. G. A. (2013). *Anatomy & physiology.*

30. Prevention, C. f. D. C. a. (2021). Post-COVID Conditions. Retrieved from https://www.cdc.gov/coronavirus/2019-ncov/long-term-effects/index.html

31. Prionas, N. D., Ray, S., & Boone, J. M. (2010). Volume assessment accuracy in computed tomography: a phantom study. *Journal of applied clinical medical physics, 11*(2), 3037-3037. doi:10.1120/jacmp.v11i2.3037

32. Riario Sforza, G. G., & Marinou, A. (2017). Hypersensitivity pneumonitis: a complex lung disease. *Clinical and molecular allergy : CMA, 15*, 6-6. doi:10.1186/s12948-017-0062-7

33. Song, F., Shi, N., Shan, F., Zhang, Z., Shen, J., Lu, H., . . . Shi, Y. (2020). Emerging 2019 Novel Coronavirus (2019-nCoV) Pneumonia. *Radiology, 295*(1), 210-217. doi:10.1148/radiol.2020200274

34. Sostre, S., Ashare, A. B., Quinones, J. D., Schieve, J. B., & Zimmerman, J. M. (1978). Thyroid scintigraphy: pinhole images versus rectilinear scans. *Radiology, 129*(3), 759-762. doi:10.1148/129.3.759

35. Vijayan, V. K. (2013). Chronic obstructive pulmonary disease. *The Indian journal of medical research, 137*(2), 251-269.

36. Waugh, A. G. A. (2022). *ROSS & WILSON ANATOMY AND PHYSIOLOGY IN HEALTH AND ILLNESS*. [S.l.]: ELSEVIER - HEALTH SCIENCE.

37. Webb, S. (1990). *From the watching of shadows : the origins of radiological tomography*. Bristol; New York: A. Hilger.

38. Wu, J., Wu, X., Zeng, W., Guo, D., Fang, Z., Chen, L., . . . Li, C. (2020). Chest CT Findings in Patients With Coronavirus Disease 2019 and Its Relationship With Clinical Features. *Invest Radiol, 55*(5).

39. Xiang, C. L. J. Z. J. G. L. Y. C. C. C. (2020). CT Findings in a Novel Coronavirus Disease (COVID-19) Pneumonia at Initial Presentation. *Biomed Res Int BioMed research international, 2020*, 5436025.

40. Xu, Z., Shi, L., Wang, Y., Zhang, J., Huang, L., Zhang, C., . . . Wang, F. S. (2020). Pathological findings of COVID-19 associated with acute respiratory distress syndrome. *Lancet Respir Med, 8*(4), 420-422. doi:10.1016/S2213-2600(20)30076-X

41. Yang, R. L. X. L. H. Z. Y. Z. X. X. Q. L. Y. G. C. Z. W. (2020). Chest CT Severity Score: An Imaging Tool for Assessing Severe COVID-19. *Radiol Cardiothorac Imaging Radiology. Cardiothoracic Imaging, 2*(2), e200047.